



Classification of aerosol-cloud interaction regimes over Tokyo

Ryohei Misumi^{a,*}, Yasushi Uji^a, Kazuhiko Miura^{b,c}, Tatsuhiro Mori^{b,d}, Yutaka Tobo^{e,f},
Yoko Iwamoto^g

^a National Research Institute for Earth Science and Disaster Resilience, Tsukuba, Japan

^b Department of Physics, Faculty of Science Division I, Tokyo University of Science, Tokyo, Japan

^c Laboratory for Environmental Research at Mount Fuji, Tokyo, Japan

^d Department of Earth and Planetary Science, Graduate School of Science, the University of Tokyo, Tokyo, Japan

^e National Institute of Polar Research, Tachikawa, Japan

^f The Graduate University for Advanced Studies, SOKENDAI, Tachikawa, Japan

^g Graduate School of Integrated Sciences for Life, Hiroshima University, Higashi-Hiroshima, Japan

ARTICLE INFO

Keywords:

Cloud droplet
Aerosol-indirect effect
Aerosol-limited regime
Tokyo Skytree

ABSTRACT

Previous studies on the aerosol indirect effect have demonstrated that there are three regimes (aerosol-limited, updraft-limited, and transitional regimes). However, this classification of regimes has not been widely used in field observations as it requires measurements of updraft or supersaturation near the cloud base (S_{\max}), which are not easy to perform. In this study, we attempted to classify the regimes using the effective supersaturation (S_{eff}) which is relatively easy to estimate by matching cloud droplet number concentration (N_c) and supersaturation spectra of cloud condensation nuclei. Parcel model simulations were performed to examine the suitability of S_{eff} as a proxy for S_{\max} . Further, 35 low-level cloud cases observed around 458 m over Tokyo were classified into three regimes. In the aerosol-limited regime, N_c increased more rapidly with an increment of aerosols than in the other two regimes, indicating that the regime classification using S_{eff} was sufficiently robust. The aerosol-limited regime in Tokyo appeared frequently when northerly winds prevailed, indicating the impact of local pollution sources around Tokyo on the aerosol cloud interaction. The results imply that anthropogenic aerosol emissions affect the climate of Tokyo.

1. Introduction

Since aerosol particles in the atmosphere act as cloud condensation nuclei (CCN) or ice nucleating particles, the number concentration of aerosol particles (N_a) affects the properties of clouds. Twomey (1974) demonstrated that the cloud droplet number concentration (N_c) increases and the effective radius (r_e) decreases as the number concentration of CCN (N_{CCN}) increases, resulting in an increase in cloud reflectance to shortwave radiation. This effect is referred to as the first aerosol indirect effect or the Twomey effect. As for other aerosol indirect effects, aerosols increase cloud lifetime and cloudiness (Albrecht, 1989), suppress precipitation (Rosenfeld, 2000), and reduce snowfall through the suppression of riming (Borys et al., 2003). Among these aerosol indirect effects, we focused on the Twomey effect in this study. However, the relationship between N_a and N_c is not linear, and the rate of increase in N_c becomes smaller when N_a is extremely large (Feingold et al., 2001). This is due to a competition effect of CCN, where an increase of N_c

reduces supersaturation and suppresses cloud droplet formation. It has also been attributed, in part, to buffering effects in aerosol-cloud interactions (Stevens and Feingold, 2009).

Based on the results of parcel model simulations, Reutter et al. (2009) classified the formation of N_c into three aerosol-cloud interaction (ACI) regimes (aerosol-limited, updraft-limited, and transitional regimes). Under the aerosol-limited regime, the ratio of updraft (w) to N_a is large ($w/N_a > \approx 10^{-3} \text{ m s}^{-1} \text{ cm}^3$) and the maximum supersaturation near the cloud base (S_{\max}) is large ($S_{\max} > \approx 0.5\%$). Under this regime, the variability of N_c is dominated mainly by N_a . In the updraft-limited regime, w/N_a is small ($w/N_a < \approx 10^{-4} \text{ m s}^{-1} \text{ cm}^3$) and S_{\max} is small ($S_{\max} < \approx 0.2\%$). Under this regime, the variation of N_c is dominated mainly by w . The transitional regime is intermediate between the two regimes. The existence of such regimes is also supported by observations. For example, in aircraft observation performed of the coast of California, Hudson and Noble (2014) showed that the variability of N_c depends more on w than on N_{CCN} when N_{CCN} is larger than 400 cm^{-3} ,

* Corresponding author at: National Research Institute for Earth Science and Disaster Resilience, 3-1 Tennodai, Tsukuba 305-006, Japan.

E-mail address: misumi@bosai.go.jp (R. Misumi).

<https://doi.org/10.1016/j.atmosres.2022.106150>

Received 2 November 2021; Received in revised form 18 March 2022; Accepted 19 March 2022

Available online 22 March 2022

0169-8095/© 2022 The Authors. Published by Elsevier B.V. This is an open access article under the CC BY license (<http://creativecommons.org/licenses/by/4.0/>).

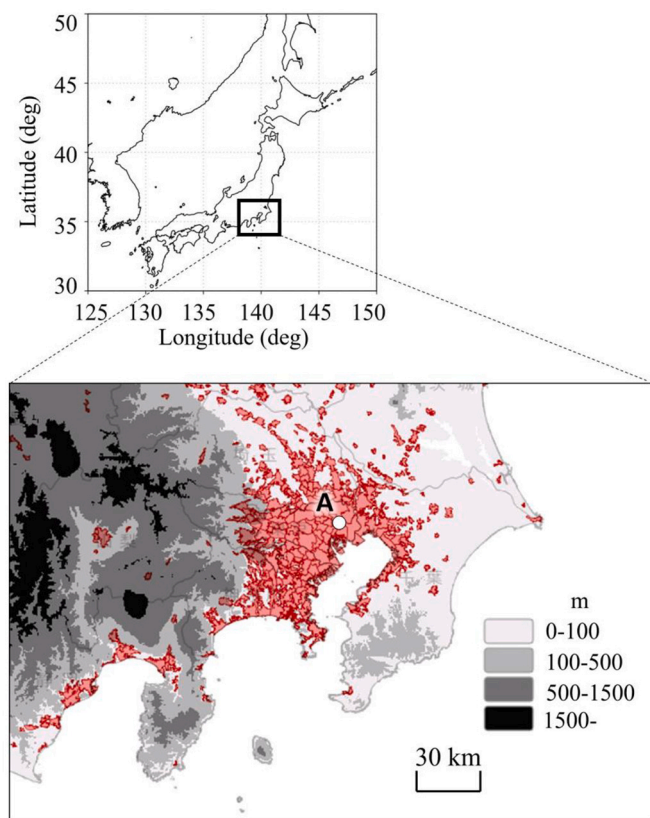


Fig. 1. Location of Tokyo Skytree (A). Gray-shaded and red areas indicate elevations and areas where the population density is greater than 4000 people/km², respectively (after the GSI map of the Geospatial Information Authority of Japan). (For interpretation of the references to colour in this figure legend, the reader is referred to the web version of this article.)

indicating the existence of the updraft-limited regime. In aircraft observations conducted over Oklahoma, Jia et al. (2019) showed that ACI acted more strongly in stratocumulus clouds than in cumulus clouds suggesting that the ACI regimes differed between the two types of clouds.

It is important to consider these regimes when discussing indirect aerosol effects, because the Twomey effect does not act strongly under the updraft-limited regime even if N_a fluctuates; however, N_c responds to N_a more sensitively under the aerosol-limited regime. To study the impact of aerosols on climate, it is important to clarify whether the Twomey effect is active or if it has been saturated. In Tokyo, aerosol concentrations have decreased significantly in recent years (e.g., Wakamatsu et al., 2013; Mori et al., 2020), and their impacts on the climate is thus an interesting scientific subject. Consequently, classification of the ACI regimes over Tokyo is important for clarifying aerosol impacts on local climate over a major urban area.

Satellite-based remote sensing has been used to classify the regimes using aerosol optical thickness (AOT). Koren et al. (2014) showed that aerosol indirect effects act strongly in regions where AOT is extremely low (e.g., “horse latitudes” in the southern hemisphere). Zhao et al. (2018a) attempted to classify the regimes around the world using long-term observations of AOT by satellites. However, precise regime classification was difficult as not only N_a but also w or S_{\max} need to be determined; however, these parameters are not easy to determine. Several methods have been proposed to estimate S_{\max} by ground-based observation; for example, measuring the threshold diameter of activating aerosols and then applying this threshold to κ -Köhler theory (Hammer et al., 2014; Iwamoto et al., 2021), or by estimating updraft using a cloud radar (Yang et al., 2019). However, these methods require

determination of the size distributions for total and interstitial aerosol particles or w , which are not easy to obtain.

In this study, the effective supersaturation (S_{eff}) were used to classify the regimes of aerosol indirect effects. The value of S_{eff} is obtained by matching the supersaturation spectra of CCN (the relationship between supersaturation and the CCN number concentration) and observed N_c (Hudson and Noble, 2014). First, parcel model simulations are performed to show that S_{eff} is useful as a proxy indicator for S_{\max} . Next, the regime classification is applied using S_{eff} to low-level clouds observed from Tokyo Skytree. Finally, favorable atmospheric conditions for aerosol-limited regimes to appear in Tokyo are discussed.

2. Instrumentation, data and methodology

2.1. Observation

The observations of cloud droplets and aerosol particles were carried out at the 458 m level of Tokyo Skytree (35.71°N, 139.81°E, 460 m above sea level, Fig. 1). At a height of 634 m, Tokyo Skytree is the tallest broadcasting tower in the world, and the upper parts of the tower are often covered by low-level clouds. Continuous observations of clouds and aerosols have been performed at the observation site since 2016 (Misumi et al., 2018; Uetake et al., 2019; Tobo et al., 2020). Similar tower-based aerosol and cloud observations are also carried out at the Puijo Tower in Finland (Portin et al., 2009; Ahmad et al., 2013), but Tokyo Skytree is unique in that it is situated in the center of a mega city. The population of Tokyo is 12 million people who are spread at a high density of more than 4000 people/km² around the observation site (Fig. 1). Anthropogenic aerosol particles prevail near the ground surface (Mochida et al., 2006; Kuwata and Kondo, 2008; Kondo et al., 2010), but occasionally clean air containing relatively fewer aerosol particles is advected from the Pacific Ocean. Regarding seasonal variations in the concentration of aerosol particles over time, in the 1980s, the concentration was typically high in winter and low in summer (Miura and Sekikawa, 1990); however, this tendency has changed in recent years, and minimum aerosol concentrations are now typically observed in the winter season (Miura, 2021).

At the 458-m level of Tokyo Skytree, cloud droplets are observed by the Fog Monitor (FM-120, Droplet Measurement Technologies Inc., USA), which is a forward-scattering spectrometer probe that uses a laser with a wavelength of 0.658 μm . The advantage of the Fog Monitor is that the sensor is installed in a wind tunnel and does not require an external pump and anemometer, which is necessary for ground-based observations using cloud droplet probes designed for aircrafts. This design makes the Fog Monitor suitable for long-term ground-based observations. Ambient air is pumped into the instrument at a rate of 1 m³ min⁻¹ and the number concentration of cloud droplets is measured. The instrument measures cloud droplets in the range of 2–50 μm sized into 30 bins. The inlet is fixed horizontally and directed to the west. One of the error sources of this instrument is particle loss during observations (Spiegel et al., 2012), but no correction has been made to our observation data as most of the cloud droplets sampled from Tokyo Skytree are less than 10 μm in diameter (Misumi et al., 2018), and the effects of particle loss on N_c is considered to be small. The data were averaged every minute and converted into an n th-order moment, M_n , which is defined as follows:

$$M_n = \int_0^\infty D^n n(D) dD \quad (1)$$

where $n(D)$ is the number concentration of droplets with diameters between D and $D + dD$. Using Eq. (1), LWC and r_c can be obtained using the equation:

$$\text{LWC} = \frac{\pi}{6} \rho_w M_3 \quad (2)$$

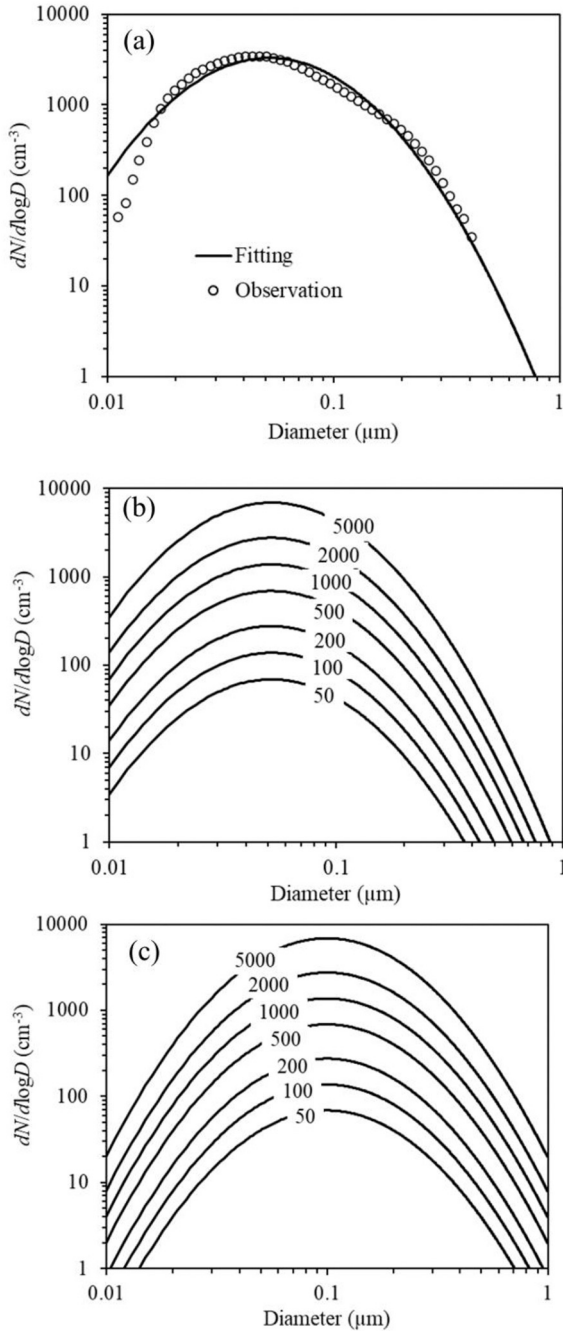


Fig. 2. (a) Mean aerosol particle size distributions observed by a Scanning Mobility Particle Sizer at the 458-m level of Tokyo Skytree from 12 December 2019 to 29 September 2020 (open circles) and a fitting line using a log-normal distribution when $D_{\log} = 0.0521 \mu\text{m}$ and $\sigma_{\log} = 0.673$. (b) Log-normal size distributions when $D_{\log} = 0.0521 \mu\text{m}$, $\sigma_{\log} = 0.673$, and $N_a = 50, 100, 200, 500, 1000, 2000$, and 5000 . (c) Same as (b) except that $D_{\log} = 0.1 \mu\text{m}$.

$$r_e = \frac{M_3}{2M_2} \quad (3)$$

where ρ_w is the density of water.

The CCN number concentration is measured by a CCN counter (CCN-100, Droplet Measurement Technologies Inc., USA). This instrument automatically measures the number concentration of CCN at a specific supersaturation level. The principle of measurements is described in detail in Roberts and Nenes (2005). The air is drawn from the outside through a 7.37-m long conductive tube with a diameter of 9.5 mm at a

rate of 1.445 L min^{-1} and a 0.2-m long, 6.4 mm tube at a rate of 0.463 L min^{-1} (see schematic diagram shown in Fig. S1a). The air containing the cloud droplets is dried in a diffusion dryer filled with silica gel which reduces the relative humidity of the sampled air to less than 35% before entering the CCN counter. In this way, the N_{CCN} in interstitial aerosols and cloud residuals are measured. The transmission efficiency of particles in this sampling system was calculated as described in Kulkarni et al. (2011) and assuming that spherical ammonium sulfate were aerosol particles. As a result, the transmission efficiencies were greater than 0.8 for particles with a diameter range of between 0.03 and $1 \mu\text{m}$ (Fig. S1b). Particles smaller and larger than this diameter range were lost due to the Brownian diffusion and inertial impaction, respectively. When the average aerosol particle size distribution observed at Tokyo Skytree (Fig. 2a) is applied, this system samples 89% of the total number of aerosol particles with the diameter ranging between $0.01 \mu\text{m}$ and $1 \mu\text{m}$. The supersaturation levels are set to 0.1%, 0.2%, 0.5%, and 0.8%. To stabilize measurements over extended periods, measurements are conducted at 30-min intervals for each supersaturation level (i.e., 2-h cycles). The instrument is calibrated using ammonium sulfate particles. The data are interpolated into 1-min intervals and then averaged for each cloud case which will be defined in section 2.3.

In order to exclude rainfall cases from the analysis, the precipitation intensity from the Extended Radar Information Network (XRAIN; Godo et al., 2014) in 2018 and 2019, and that observed by a laser precipitation monitor (LPM, Adolf Theis GmbH & Co.KG, Germany) installed after 2020 at the 458-m level of Tokyo Skytree are used. The temperature and wind at the 1000-hPa, 975-hPa, and 950-hPa levels of the initial values of the JMA Mesoscale Model forecast provided at 3-h intervals are used to investigate the mesoscale meteorological conditions around the observation site. These data are linearly interpolated and averaged for each cloud event. For an analysis of air mass trajectories, the Hybrid Single-Particle Lagrangian Integrated Trajectory model (HYSPLIT; Stein et al., 2015; Rolph et al., 2017) is used. The trajectories are calculated using the Global Data Assimilation System (GDAS) with a spatial resolution of $1^\circ \times 1^\circ$ in longitude and latitude. In order to examine the impacts of preceding precipitation on the regime classification, the accumulated precipitation along trajectories (APT; Dadashazar et al., 2021) is calculated by integrating the surface precipitation from the GDAS over 24 h prior to the air mass reaching the observation point.

2.2. Estimation of effective supersaturation

In general, small aerosol particles can be activated to form cloud droplets when the supersaturation is large. Therefore, S_{max} is an important factor affecting N_c ; however, measuring S_{max} is still difficult. In this study, we used the effective supersaturation (Hudson and Noble, 2014) as a proxy indicator for S_{max} , which is defined as:

$$N_{\text{CCN}}(S_{\text{eff}}) = N_{c_{\text{max}}} \quad (4)$$

where, N_{CCN} indicates the number concentration of CCN, which is a function of the supersaturation, and $N_{c_{\text{max}}}$ is the 95th percentile of N_c . The reason for using $N_{c_{\text{max}}}$ is to calculate S_{eff} for less diluted airmasses. Note that $N_{c_{\text{max}}}$ is uniquely determined for each cloud event; that is, one S_{eff} is determined for each cloud event. For the supersaturation spectra of CCN, the N_{CCN} measured by the CCN counter is fitted with the function given by Khvorostyanov and Curry (2006) as:

$$N_{\text{CCN}}(S) = C_0 S^k (1 + \eta_0 S^k)^{-1} \quad (5)$$

where, S is the supersaturation, and C_0 , η_0 and k are constants. The value of S_{eff} can be estimated by solving the following equation obtained from (4) and (5) as:

$$S_{\text{eff}} = \left(\frac{N_{c_{\text{max}}}}{C_0 - \eta_0 N_{c_{\text{max}}}} \right)^{1/k} \quad (6)$$

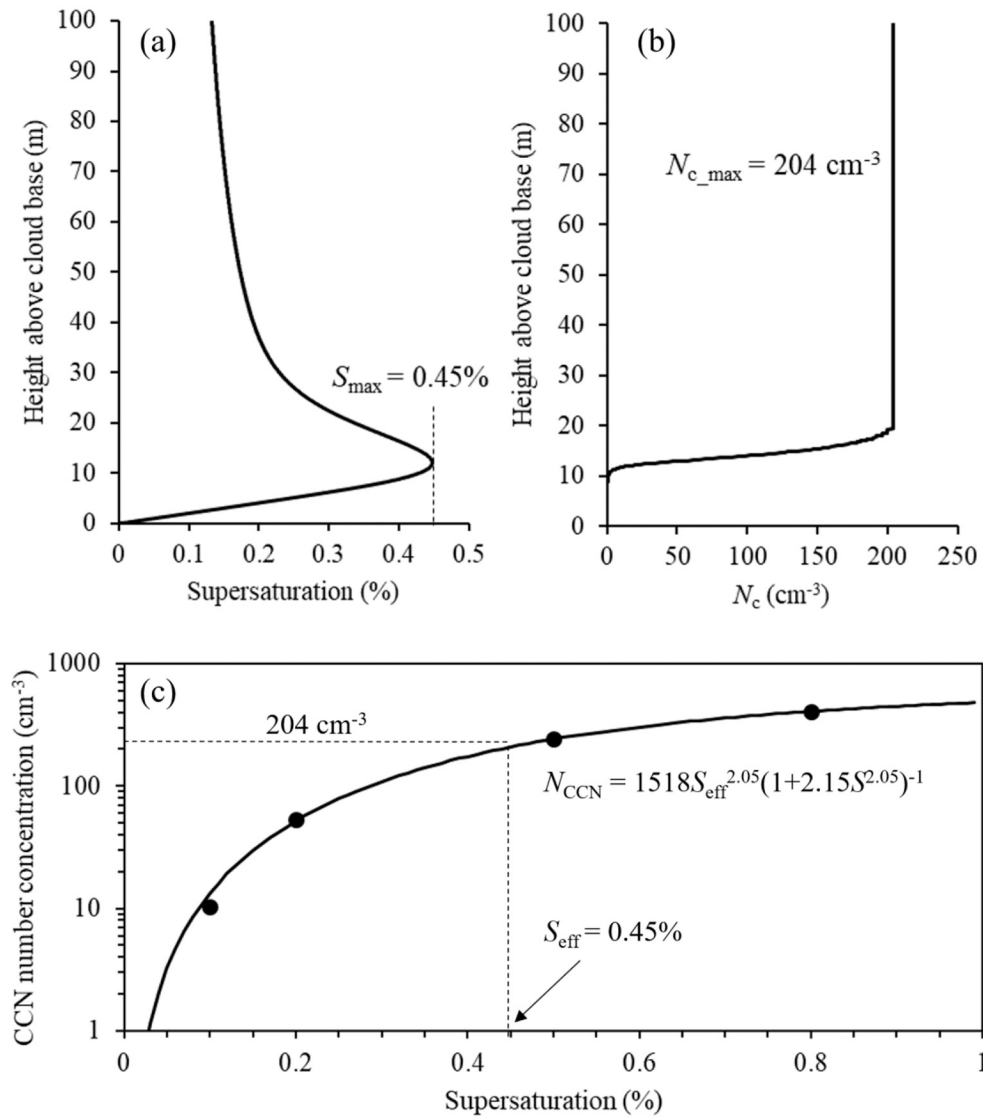


Fig. 3. Vertical profiles of (a) supersaturation and (b) N_c simulated by the parcel model for $\kappa = 0.1$, $N_a = 1000 \text{ cm}^{-3}$, and $w = 1.0 \text{ m s}^{-1}$. (c) The supersaturation spectrum of CCN for this case.

In order to examine how well S_{eff} reflects S_{max} , parcel model simulations are performed. The purpose of the simulations is to verify the validity of using S_{eff} as a proxy for S_{max} under hypothetical conditions varying supersaturation and hygroscopicity. The model represents an adiabatically rising air parcel without entrainment. The activation of CCN and condensation growth of cloud droplets are calculated using κ -Köhler theory (Petters and Kreidenweis, 2007). Equations of the parcel model are similar to those in Rothenberg and Wang (2016) and details of the model are described in the Supplementary Material. The initial aerosol particle size distribution is assumed to have a log-normal distribution as:

$$n(D) = \frac{N_a}{\sqrt{2\pi}\sigma_{\log}D} \exp\left\{-\frac{[\ln(D/D_{\log})]^2}{2\sigma_{\log}^2}\right\} \quad (7)$$

where, N_a is the number concentration of total aerosol particles, and D_{\log} and σ_{\log} are parameters related to the median diameter and the width of the particle size distribution spectrum, respectively. The values of D_{\log} and σ_{\log} are given as 0.0521 μm and 0.673, respectively, based on the mean aerosol particle size distributions observed by the Tokyo University of Science at the 458-m level of Tokyo Skytree using a Scanning

Mobility Particle Sizer (SMPS3938L52, TSI Inc., USA) from 12 December 2019 to 29 September 2020 (open circles in Fig. 2a). In order to perform calculations for various particle size distributions, N_a is set to 50, 100, 200, 500, 1000, 2000, and 5000 cm^{-3} (Fig. 2b), and D_{\log} is set to 0.0521 and 0.1 μm (Fig. 2b and c). According to previous observations, the hygroscopicity parameter κ in Japan ranges from 0.08 to 0.38 in median values in Tsukuba (Orikasa et al., 2020), from 0.13 to 0.42 on the Noto Peninsula (Iwamoto et al., 2016), and from 0.1 to 0.4 in summer in Tokyo (Ohata et al., 2016). In this simulation, κ is fixed at 0.1, 0.3, and 0.5.

The supersaturation spectrum of CCN (Eq. (4)) was created by running the parcel model with constant supersaturation set at 0.1%, 0.2%, 0.5%, and 0.8% in the same way as actual observations are performed by the CCN counter. Next, S_{eff} is calculated using the maximum N_c simulated by the parcel model. Then, the obtained S_{eff} is compared with S_{max} . A total 294 cases were run by changing κ to 0.1, 0.3, and 0.5, N_a as 50, 100, 200, 500, 1000, 2000, and 5000 cm^{-3} , w to 0.1, 0.2, 0.5, 0.75, 1, 2, 5 m s^{-1} , and D_{\log} to 0.0521 and 0.1 μm . Since meteorological conditions at the cloud bases were not observed, hypothetical initial conditions of 20 °C temperature, 100% relative humidity and constant updrafts were used in the simulation. The calculations were performed

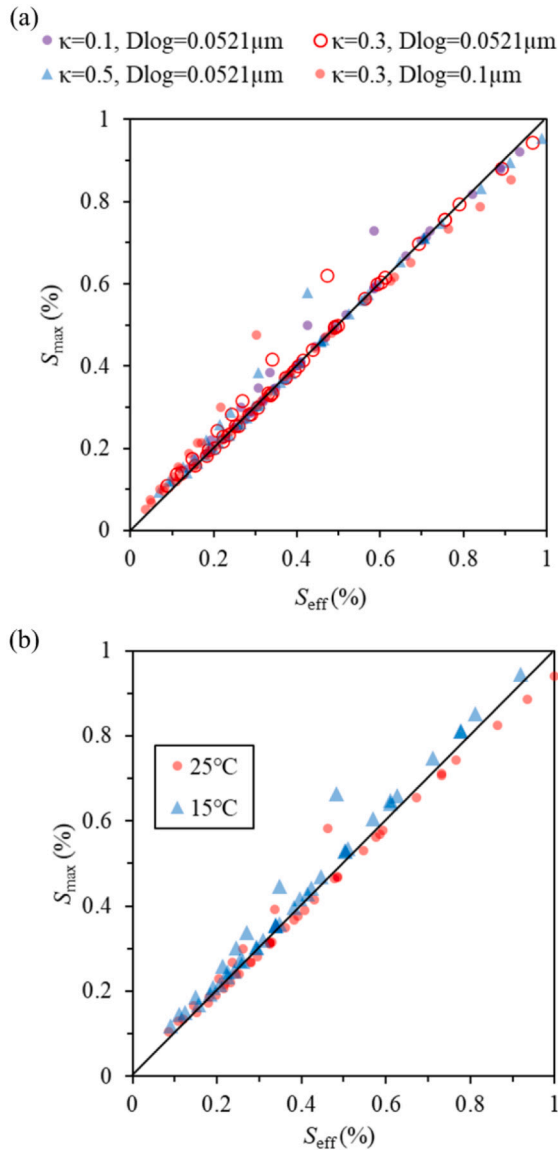


Fig. 4. Relationship between S_{eff} and S_{max} in the parcel model simulations (a) for different κ and D_{log} values, and (b) assuming the initial parcel temperature as 15 °C and 25 °C when $\kappa = 0.3$ and $D_{\text{log}} = 0.0521 \mu\text{m}$. Data were plotted only for cases where S_{eff} and S_{max} are less than 1.0 (172 and 87 cases in (a) and (b), respectively). Solid lines indicate $S_{\text{eff}} = S_{\text{max}}$.

until the parcel reached 100 m above the cloud base. In control runs, the initial temperature of the parcel was fixed, but sensitivity tests involving the initial temperature ± 5 K were also performed. In order to remove haze particles, cloud droplets greater than $5 \mu\text{m}$ in diameter were counted as N_c .

Fig. 3 shows the vertical profiles of supersaturation and N_c when $\kappa = 0.1$, $N_a = 1000 \text{ cm}^{-3}$, and $w = 1.0 \text{ m s}^{-1}$ calculated by the parcel model. The supersaturation increased as the parcel rose from the cloud base and reached $S_{\text{max}} = 0.45\%$ at the 12-m level from the cloud base (Fig. 3a). Above this height, N_c became a constant value ($= 204 \text{ cm}^{-3}$), indicating that the condensed water was used for the growth of cloud droplets (Fig. 3b). Substituting 204 cm^{-3} as $N_{c,\text{max}}$ in Eq. (6), $S_{\text{eff}} = 0.45\%$ was obtained (Fig. 3c). In this calculation, S_{eff} was the same as S_{max} , but they were not always equal in other cases. Fig. 4a shows the relationship between S_{eff} and S_{max} for the 172 parcel model simulations where S_{eff} and S_{max} were less than 1.0. The values of S_{eff} and S_{max} are in good agreement, and most plots are close to the line of $S_{\text{eff}} = S_{\text{max}}$ with a few

exceptions. The mean absolute error of S_{eff} relative to S_{max} was 0.015% for S_{eff} between 0.1 and 0.8, suggesting that S_{eff} can be used as a proxy index for S_{max} in this range. The effect of κ on the $S_{\text{eff}} - S_{\text{max}}$ relation is small.

However, this is the result from the parcel model simulation performed under ideal conditions, and there are various error sources in actual observations. One possible error is the effect of temperature. In our observations, supersaturation spectra were observed at the temperature inside the CCN counter installed at an altitude of 458 m, which was higher than the cloud base. Therefore, the temperature was different between the observation site and the cloud base. In order to investigate this effect, simulations were performed by changing the cloud-base temperature by ± 5 K using the same supersaturation spectra (Fig. 4b). The results show a tendency for $S_{\text{eff}} > S_{\text{max}}$ for +5 K (25 °C) and $S_{\text{eff}} < S_{\text{max}}$ for -5 K (15 °C), but the mean absolute error of these plots was 0.024% for S_{eff} between 0.1 and 0.8. Therefore, the temperature had only a slight effect on the estimation of S_{eff} . Another possible error is that the airmasses used to observe $N_{c,\text{max}}$ were not always the same as those used to estimate N_{CCN} , because the sampling of CCN was carried out using a two-hour cycle. This error can be negligible if the temporal change in N_{CCN} is small. The mean temporal change in N_{CCN} at $S = 0.8\%$ in two hours was 30.7% in the data from April to December 2019. Such fluctuations could cause the same magnitude of errors in the estimation of S_{eff} . Therefore, cloud events, where the coefficient of variance (i.e., the ratio of the standard deviation to the mean) of N_{CCN} at $S = 0.1, 0.2, 0.5$, or 0.8% exceeded 30%, were excluded from the analysis. The errors in estimating S_{eff} caused by the variation of N_{CCN} were evaluated in all cases.

In our observations, N_{CCN} was measured after drying all of the cloud droplets, instead of measuring N_{CCN} before cloud formation. This measurement could cause another error because dissolution of chemicals after cloud formation might alter the mass of CCN. To investigate the effect of this error, we compared the N_{CCN} at 5 min before the onset of cloud events with that observed during the cloud events at 2 h later. The results show that N_{CCN} are different before and after the cloud formation, but no bias was detected (Fig. S2). It is considered that the variations of N_{CCN} due to airmass replacement during cloud events are much larger than those due to the modification of CCN after condensation, and therefore, no correction was made for this error.

2.3. Cases

Among the low-level clouds observed at Tokyo Skytree, the data obtained from March 2018 to August 2020 are examined in this study. The time used in this study is the Japan Standard Time (UTC + 9 h). Note that no data are available for September 2018 and from December 2018 to March 2019 due to problems encountered with equipment. The analyzed cases were selected based on the following criteria.

- 1) The liquid water content (LWC) observed by the Fog Monitor is greater than 0.01 g m^{-3} . This criterion is necessary to distinguish cloud events from non-cloud events such as large aerosol particles.
- 2) The precipitation intensity is less than 0.1 mm h^{-1} . This criterion minimizes the effects of wash out of cloud droplets by raindrops.
- 3) The period satisfying 1) and 2) continues more than 60 min. This criterion is to exclude short-duration clouds.
- 4) A cloud event is regarded as having terminated when 1) or 2) is not fulfilled for more than 60 min.
- 5) The value of S_{eff} calculated for the event is between 0.1 and 0.8. This criterion ensures that the difference between S_{eff} and S_{max} is small (Fig. 4).
- 6) The coefficients of variance of N_{CCN} at supersaturation at 0.1%, 0.2%, 0.5%, or 0.8% are less than 30% to avoid large errors in estimating S_{eff} .

Using these criteria, 35 cases were selected. Table 1 shows the

Table 1

List of low-level clouds observed from Tokyo Skytree. N_c , LWC, r_e , and $N_{0.8\%}$ are the mean values \pm standard deviations, and N_{c_max} is the 95th percentile of N_c . For S_{max} , the mean values and the variations corresponding to the observation errors of N_{CCN} are shown in parentheses.

Date	Time (JST)	Duration (hours)	N_c (cm^{-3})	N_{c_max} (cm^{-3})	LWC (g m^{-3})	r_e (μm)	$N_{0.8\%}$ (cm^{-3})	S_{eff} (%)
5–6 Apr 2018	21:33–4:47	7.2	201 \pm 90	344	0.20 \pm 0.14	7.1 \pm 1.7	785 \pm 167	0.34 (0.30–0.41)
15 Jun 2018	3:38–8:35	5.0	114 \pm 64	243	0.12 \pm 0.09	7.6 \pm 1.8	652 \pm 86	0.20 (0.19–0.20)
9–10 Jul 2018	23:14–03:40	4.4	211 \pm 182	622	0.05 \pm 0.04	4.1 \pm 0.3	1383 \pm 92	0.25 (0.21–0.30)
12 Aug 2018	3:03–7:05	4.0	57 \pm 27	103	0.04 \pm 0.02	6.5 \pm 1.5	520 \pm 78	0.10 (0.09–0.10)
21–22 Aug 2018	20:59–1:23	4.4	158 \pm 112	380	0.03 \pm 0.02	3.7 \pm 0.2	1151 \pm 180	0.31 (0.18–0.23)
11 Oct 2018	20:39–23:50	3.2	254 \pm 267	750	0.05 \pm 0.07	3.9 \pm 0.4	2604 \pm 232	0.18 (0.17–0.20)
12 May 2019	3:46–6:06	2.3	131 \pm 71	243	0.12 \pm 0.08	8.0 \pm 2.2	641 \pm 65	0.15 (0.14–0.20)
20 Jun 2019	5:37–7:18	1.7	162 \pm 87	342	0.06 \pm 0.02	5.1 \pm 0.7	656 \pm 5	0.17 (0.17–0.18)
29 Jun 2019	4:27–10:26	6.0	74 \pm 39	145	0.11 \pm 0.06	7.9 \pm 0.7	183 \pm 13	0.53 (0.48–0.60)
30 Jun 2019	4:37–6:40	2.1	82 \pm 32	139	0.24 \pm 0.12	11.2 \pm 2.1	495 \pm 133	0.24 (0.22–0.28)
1 Jul 2019	14:52–21:35	6.7	135 \pm 87	299	0.21 \pm 0.18	8.7 \pm 2.2	923 \pm 82	0.20 (0.19–0.21)
6 Jul 2019	5:29–7:23	1.9	124 \pm 47	231	0.04 \pm 0.02	4.3 \pm 0.3	299 \pm 10	0.55 (0.52–0.58)
11 Oct 2019	5:26–10:47	5.3	45 \pm 20	83	0.05 \pm 0.02	9.9 \pm 1.5	295 \pm 46	0.17 (0.15–0.18)
11 Oct 2019	14:44–16:50	2.1	185 \pm 48	267	0.14 \pm 0.05	6.3 \pm 1.0	471 \pm 82	0.37 (0.36–0.37)
17 Dec 2019	13:07–17:48	4.1	90 \pm 52	179	0.13 \pm 0.09	9.2 \pm 1.2	705 \pm 64	0.21 (0.19–0.21)
19 Dec 2019	19:02–23:29	4.5	73 \pm 30	130	0.04 \pm 0.02	6.3 \pm 1.0	201 \pm 22	0.45 (0.40–0.51)
16 Feb 2020	12:49–17:26	4.6	66 \pm 38	141	0.06 \pm 0.05	7.1 \pm 2.1	696 \pm 114	0.13 (0.12–0.15)
16–17 Feb 2020	22:26–4:15	5.8	187 \pm 100	393	0.04 \pm 0.02	3.9 \pm 0.7	402 \pm 23	0.78 (0.71–0.87)
20 Mar 2020	0:59–2:27	1.5	157 \pm 72	281	0.04 \pm 0.02	4.1 \pm 0.2	341 \pm 17	0.58 (0.51–0.65)
6 May 2020	11:45–15:33	3.8	93 \pm 57	195	0.06 \pm 0.03	7.3 \pm 1.6	226 \pm 23	0.66 (0.58–0.78)
16 May 2020	18:36–19:54	1.3	124 \pm 75	285	0.07 \pm 0.05	5.6 \pm 0.4	394 \pm 10	0.55 (0.52–0.56)
16–17 May 2020	23:38–3:16	3.6	91 \pm 53	197	0.07 \pm 0.07	6.1 \pm 1.1	323 \pm 33	0.46 (0.41–0.56)
22–23 May 2020	21:27–5:39	8.2	32 \pm 16	60	0.12 \pm 0.08	10.6 \pm 1.5	80 \pm 7	0.65 (0.60–0.70)
4 Jun 2020	4:58–8:03	3.1	138 \pm 103	357	0.07 \pm 0.05	6.3 \pm 1.3	743 \pm 101	0.21 (0.20–0.21)
13 Jun 2020	0:33–6:10	5.6	215 \pm 554	481	0.14 \pm 0.19	6.1 \pm 1.3	787 \pm 156	0.53 (0.48–0.57)
22 Jun 2020	13:35–17:46	4.2	156 \pm 96	378	0.04 \pm 0.03	4.1 \pm 0.3	374 \pm 29	0.81 (0.71–0.93)
25 Jun 2020	9:46–13:55	4.1	69 \pm 39	153	0.04 \pm 0.02	6.5 \pm 1.5	183 \pm 32	0.68 (0.58–0.84)
26 Jun 2020	0:32–9:57	9.2	69 \pm 32	126	0.17 \pm 0.11	10.5 \pm 2.4	784 \pm 139	0.13 (0.10–0.17)
4 Jul 2020	6:01–7:37	1.6	119 \pm 87	348	0.04 \pm 0.04	4.6 \pm 0.6	929 \pm 137	0.32 (0.29–0.37)
19–20 Jul 2020	22:25–1:34	3.1	158 \pm 68	301	0.07 \pm 0.05	5.4 \pm 0.9	917 \pm 66	0.23 (0.20–0.26)
21–22 Jul 2020	22:30–7:04	8.6	204 \pm 111	410	0.05 \pm 0.04	4.2 \pm 0.4	846 \pm 81	0.27 (0.24–0.32)
27 Jul 2020	0:44–3:53	3.2	75 \pm 39	167	0.03 \pm 0.02	4.8 \pm 0.8	255 \pm 33	0.34 (0.25–0.47)
28 Jul 2020	1:12–4:37	3.4	225 \pm 130	478	0.06 \pm 0.05	4.3 \pm 0.5	687 \pm 70	0.47 (0.41–0.56)
4 Aug 2020	4:44–6:38	1.9	192 \pm 87	414	0.03 \pm 0.02	3.8 \pm 0.3	813 \pm 57	0.32 (0.30–0.33)
5 Aug 2020	1:45–3:48	2.1	221 \pm 108	489	0.03 \pm 0.01	3.3 \pm 0.2	808 \pm 17	0.38 (0.37–0.39)

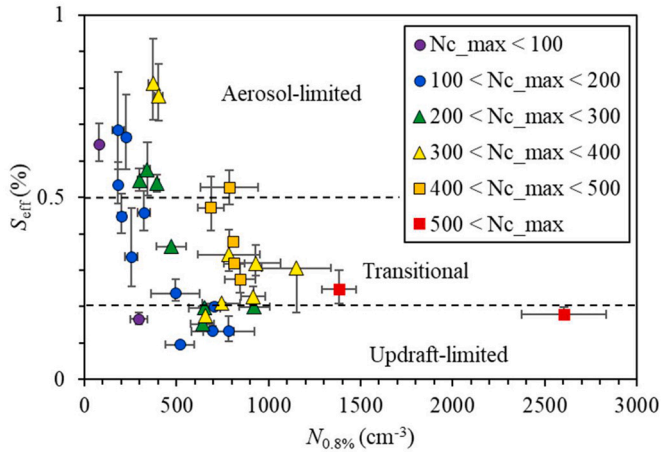


Fig. 5. Relationship between $N_{0.8\%}$ and S_{eff} for the observed 35 cases. Dashed lines indicate the boundaries of regimes. Error bars represent the standard deviations of $N_{0.8\%}$ and the errors in estimating S_{eff} due to the observation errors in N_{CCN} .

sampling date and time of each event, their duration, the mean values and the standard deviations for N_c , LWC, the effective radius (r_e) of cloud droplets, and N_{CCN} at 0.8% supersaturation ($N_{0.8\%}$), and the values of N_{c_max} and S_{eff} . The observed clouds are low-level stratiform clouds, which appear frequently under the following conditions: the first condition is when moist northeasterly winds blow from the Pacific Ocean, the second condition is when moist southwesterly winds from cyclonic

systems over the Pacific Ocean prevail over Tokyo, and the third condition is when frontal systems approach Tokyo. It should be noted that 74% of the cases were observed between May and September, which means that there is a seasonal bias in our observations. In addition, 77% of the low-level clouds appeared between 18 and 06 JST, indicating that the clouds at the top of the boundary layer are likely to form at nighttime (e.g., [Oliver et al., 1978](#)).

3. Results

3.1. Regime classification

Fig. 5 shows scatter plots of $N_{0.8\%}$ vs S_{eff} for the 35 cases. Here, $N_{0.8\%}$ is used as an index of aerosol number concentration since N_{CCN} at a high supersaturation reflects the total number of aerosol particles. Thus, $N_{0.8\%}$ is used instead of N_a in this study. N_{c_max} tends to show large values when $N_{0.8\%}$ increases, suggesting that the Twomey effect affects N_{c_max} . We classify the 35 cases into three regimes. According to [Reutter et al. \(2009\)](#), an aerosol-limited regime is characterized by high w/N_a ratios ($> \approx 10^{-3} \text{ ms}^{-1} \text{ cm}^3$), high S_{max} ($S_{max} > \approx 0.5\%$), and high activated fractions of aerosol particles ($N_c/N_a > \approx 90\%$), while an updraft-limited regime is characterized by low w/N_a ratios ($< \approx 10^{-4} \text{ ms}^{-1} \text{ cm}^3$), low S_{max} ($< \approx 0.2\%$), and low N_c/N_a ($< \approx 20\%$). A transitional regime is characterized by parameter values in between the two other regimes. In the present study, we attempt to use S_{eff} to classify the three regimes; that is, $S_{eff} \geq 0.5\%$ as the aerosol-limited regime, $0.2 \leq S_{eff} < 0.5\%$ as the transitional regime, and $S_{eff} < 0.2\%$ as the updraft-limited regime. Here S_{eff} is used instead of S_{max} since the difference between S_{eff} and S_{max} was small according to the parcel model simulation (**Fig. 4**). As a result, the 35 cases are classified into 10 cases of aerosol-limited regimes (29%), 16

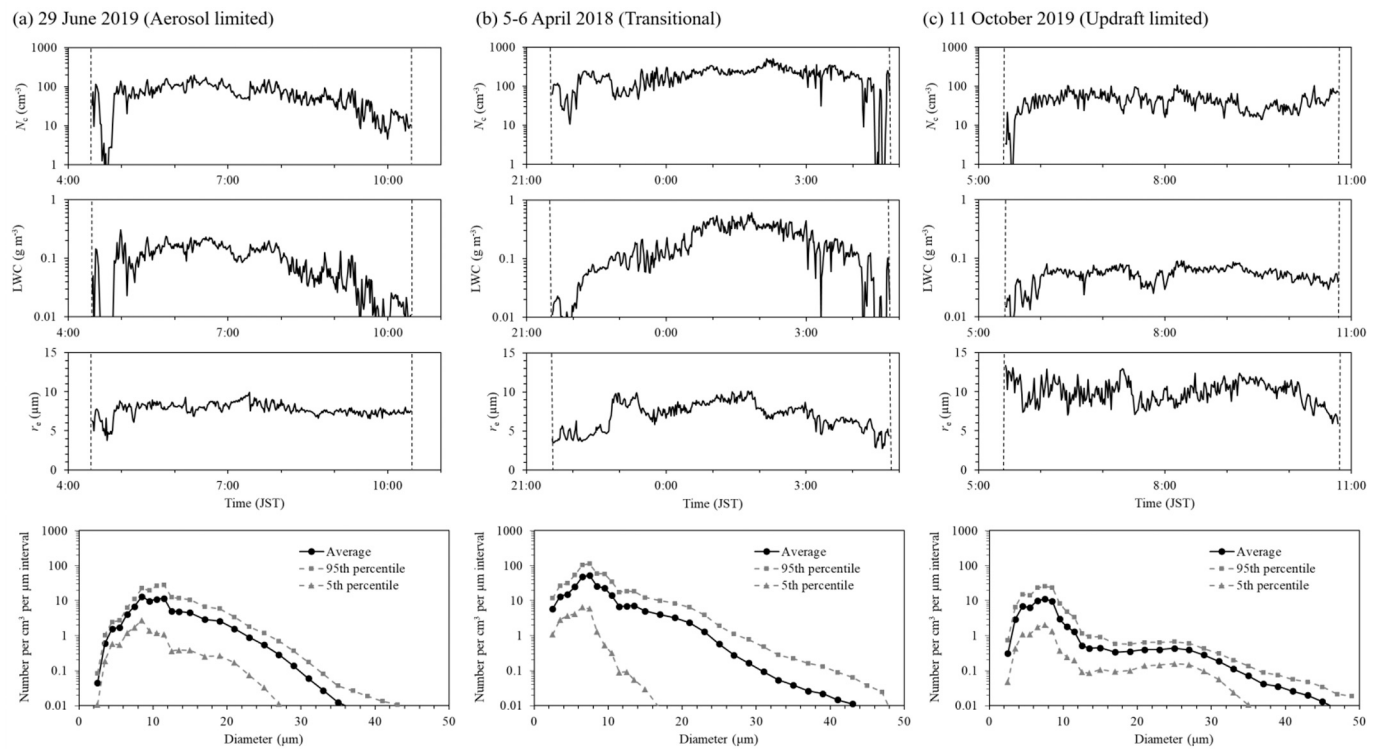


Fig. 6. Time variations N_c , LWC, r_e , and the mean cloud droplet size distributions with the 5th and 95th percentile values for cloud events on (a) 29 June 2019 (aerosol-limited regime), (b) 5–6 April 2018 (transitional regime), and (c) 11 October 2019 (updraft limited regime).

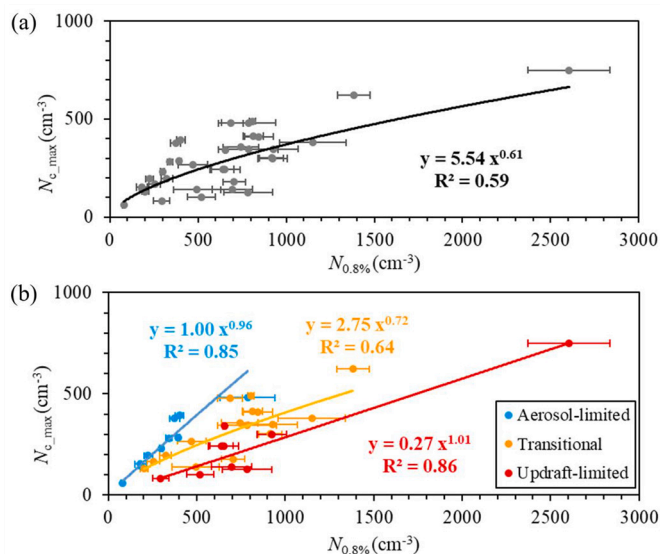


Fig. 7. Relationship between $N_{0.8\%}$ and $N_{c,max}$ for (a) all cases and (b) each regime. Solid lines represent power regressions, and error bars indicate standard deviations of $N_{0.8\%}$.

cases of transitional regimes (46%), and 9 cases of updraft-limited regimes (16%). When the errors in S_{eff} associated with the variation in the N_{CCN} of each event are taken into account, the number of cases varied from 8 to 13 (23–37%) for the aerosol-limited regime, 15 to 17 (43–49%) for the transitional regime, and 7 to 10 (20–29%) for the updraft-limited regime.

Fig. 6 shows the temporal variation of N_c , LWC, and r_e and the mean cloud droplet size distributions for three cases with one case from each of the three regimes. In all cases, LWC larger than 0.01 g m^{-3} were

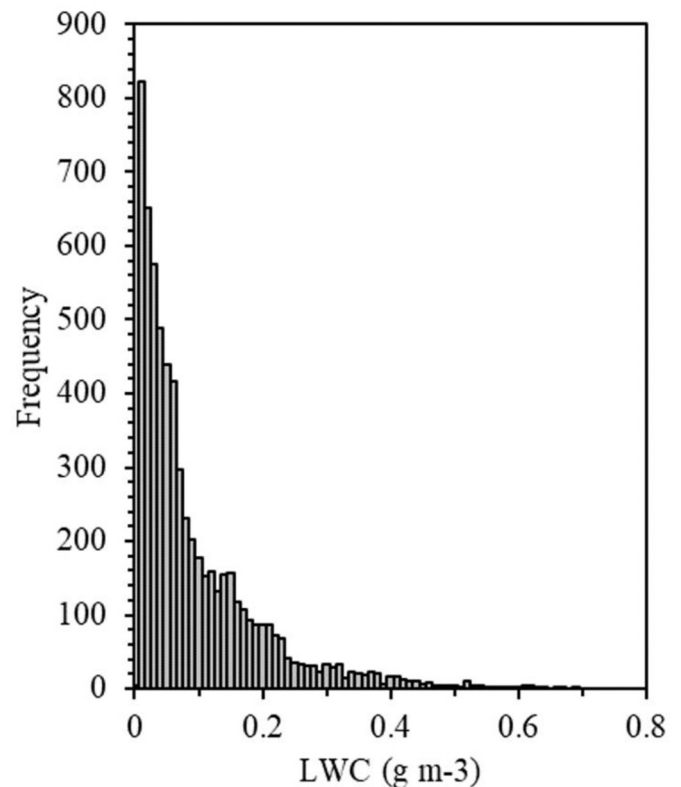


Fig. 8. Frequency distribution of LWC for all samplings.

observed continuously over several hours reflecting stratiform clouds. In the three cases, the mean N_c ($201 \pm 90 \text{ cm}^{-3}$) and LWC ($0.20 \pm 0.14 \text{ g m}^{-3}$) were largest on 5–6 April 2018 (Fig. 6b), while the mean r_e was

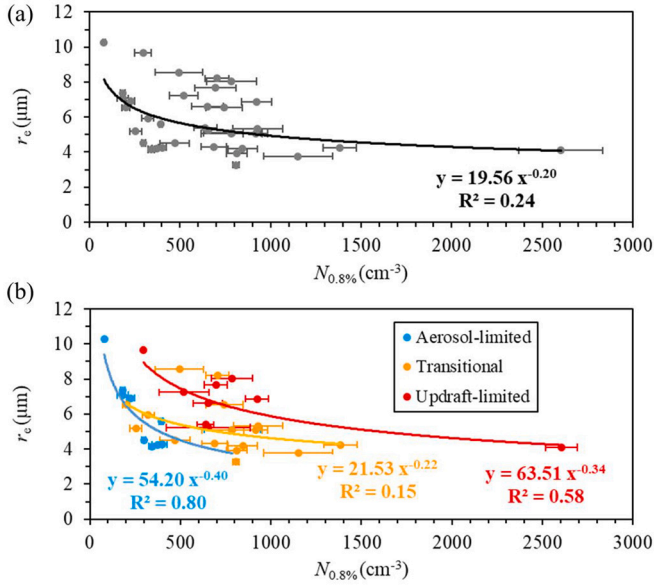


Fig. 9. Relationships between $N_{0.8\%}$ and r_e averaged between $LWC = 0.4\text{--}0.6\text{ g m}^{-3}$ for (a) all cases and (b) each regime. Solid lines represent power regressions, and error bars indicate standard deviations of $N_{0.8\%}$.

Table 2

ACI_N and ACI_r for the three regimes and for all cases.

Regimes	ACI_N	ACI_r ($LWC = 0.04\text{--}0.06\text{ g m}^{-3}$)
Aerosol-limited	0.32	0.40
Transitional	0.24	0.22
Updraft-limited	0.34	0.34
All	0.20	0.20

largest on 11 October 2019 ($9.9 \pm 1.5\text{ }\mu\text{m}$; Fig. 6c). The mean cloud particle size distributions had peaks in the diameter range between 6.5 and 8.5 μm , and the maximum cloud droplet sizes were between 35 and 46 μm .

The relationship between $N_{0.8\%}$ and $N_{c,max}$ for all cloud events is shown in Fig. 7a. The values of $N_{c,max}$ increase with $N_{0.8\%}$, but the coefficient of determination is relatively small ($R^2 = 0.59$). When the data are restricted to the aerosol-limited regime, the slope of the regression line increases to 1.0 with $R^2 = 0.85$ (Fig. 7b). This indicates that $N_{c,max}$ increases rapidly with increasing $N_{0.8\%}$ in this regime, suggesting that the regime classification using S_{eff} performs properly. The slope of the regression lines is relatively small in the other two regimes, indicating that $N_{c,max}$ is less sensitive to an increase in aerosols.

In studies of aerosol impacts on r_e , a narrow LWC range is sometimes applied to avoid the effects of LWC variations (e.g., Ansari et al., 2020). The frequency distribution of LWC observed in this study is shown in Fig. 8. Large amounts of data exist when LWC is small, while data are scarce when LWC is large. Especially, the amount of data in $LWC > 0.1\text{ g m}^{-3}$ is extremely small. Considering the statistical significance, LWC ranges including many data should be used, but a small value of LWC should not be used because it corresponds to undeveloped cloud areas. Here, r_e was averaged in the range between $LWC = 0.04$ and 0.06 g m^{-3} (Fig. 9). For comparison, r_e averaged in the range between $LWC = 0.08\text{--}0.10\text{ g m}^{-3}$ was also examined (Fig. S3), but the result was not significantly different. For all cloud events, r_e decreases with increasing $N_{0.8\%}$. However, the coefficient of determination is only $R^2 = 0.24$. When the data are restricted to the aerosol-limited regime, r_e tends to decrease more rapidly than in the two other regimes. Here, aerosol-cloud interaction (ACI) is quantified by the method of McComiskey

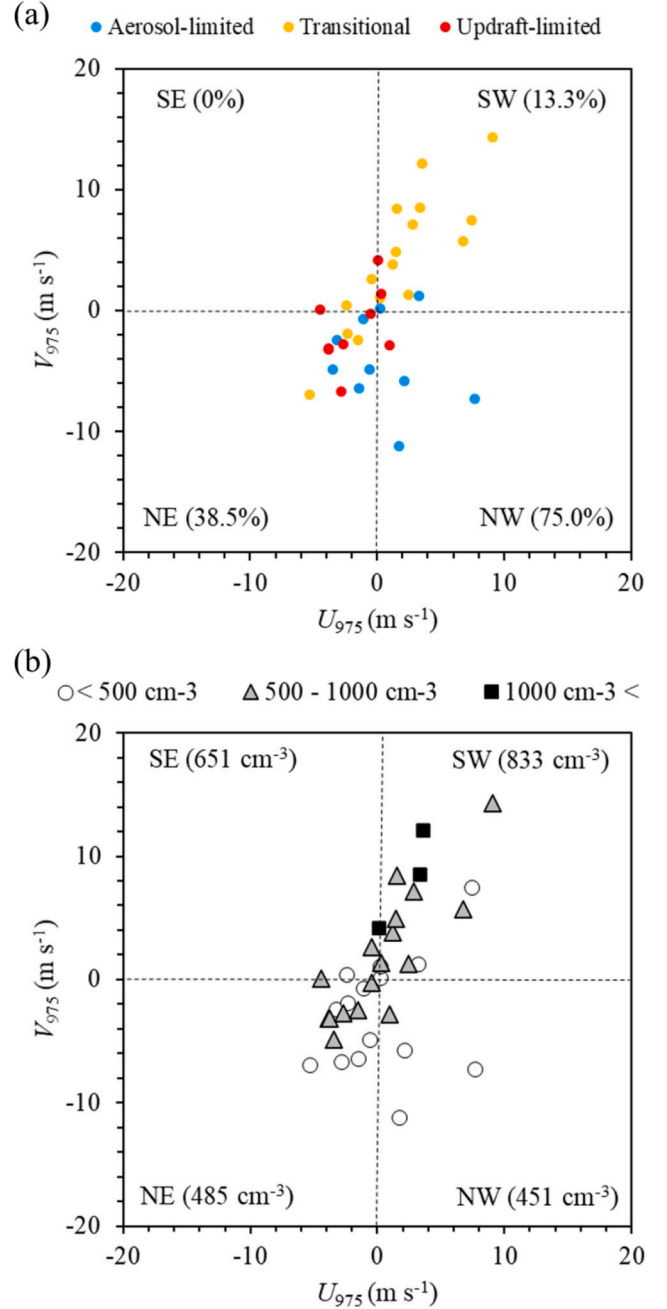


Fig. 10. Dependencies of (a) regime classification and (b) $N_{0.8\%}$ on the west to east (U_{975}) and the south to north (V_{975}) wind components at the 975-hPa level. Numerals in parentheses indicate (a) percentage of aerosol-limited regime and (b) the mean values of $N_{0.8\%}$ in each wind-direction quadrant.

and Feingold (2012) as follows:

$$ACI_N = \frac{1}{3} \left(\frac{\partial \ln N_c}{\partial \ln \alpha} \right) \quad (8)$$

$$ACI_r = - \left(\frac{\partial \ln r_e}{\partial \ln \alpha} \right)_{LWC} \quad (9)$$

where, α is the amount of aerosol. In this study $N_{0.8\%}$ is used for α , and $N_{c,max}$ is substituted for N_c in Eq. (8). For all cloud events, $ACI_N = 0.20$ and $ACI_r = 0.20$ are obtained (Table 2). According to McComiskey and Feingold (2012), the relationship $ACI_N = ACI_r$ holds, and the values range between 0.04 and 0.33. Comparing our results to the list of ACI

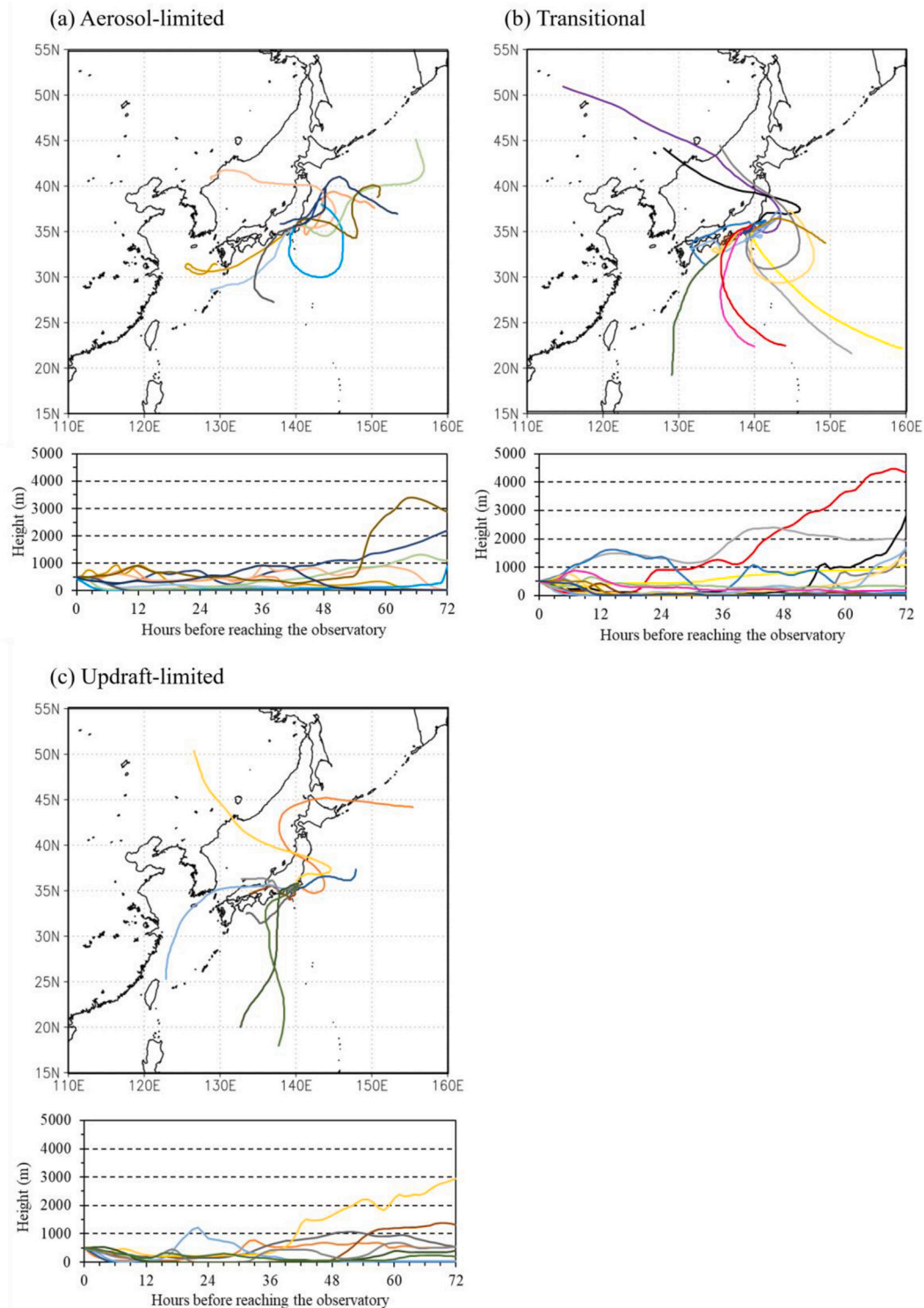


Fig. 11. Trajectories of airmasses for 72 h prior to the onset of cloud events for (a) aerosol-limited, (b) transitional, and (c) updraft-limited regimes.

values observed around the world by [McComiskey and Feingold \(2012\)](#), the values of ACI_N and ACI_r are in their range. In recent observations of ACI in East Asia, $ACI_r = 0.025\text{--}0.261$ in Mt. Tai in the northeast China ([Li et al., 2020](#)), $ACI_r = 0.10\text{--}0.19$ in Hebei ([Zhao et al., 2018a, 2018b](#)), and $ACI_N = 0.245$ and $ACI_r = 0.16$ in the Loess Plateau ([Cai et al., 2022](#)) are obtained, which are not very different from our results. On the other hand, in observations in the Western Ghats, India, $AIE_N = 0.073\text{--}0.08$ and $AIE_r = 0.06\text{--}0.077$ were obtained ([Ansari et al., 2020](#)), which are considerably smaller than our results. Their findings could be attributed

to their observations being performed using a wider range of N_{CCN} ($500\text{--}7000\text{ cm}^{-3}$) compared to the range employed in our study, suggesting that their observations were performed under a more polluted atmosphere.

It should be noted that the values obtained for ACI_N and ACI_r for each regime are relatively high compared to those obtained for all cases ([Table 2](#)); for example, $ACI_N = 0.34$ and $ACI_r = 0.40$ was obtained under the aerosol limited regime, and $ACI_N = ACI_r = 0.34$ under the updraft limited regime. These findings indicate that the relationship between

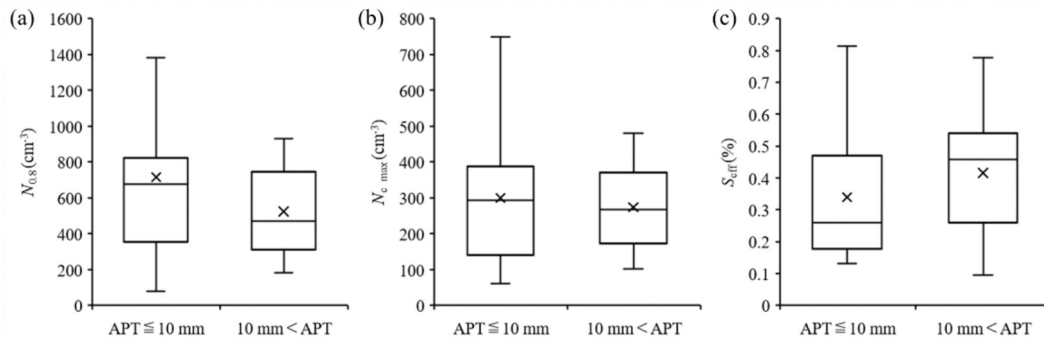


Fig. 12. Box plots of (a) $N_{0.8\%}$, (b) $N_{c,max}$, and (c) S_{eff} for $APT \leq 10$ mm and $APT > 10$ mm.

$N_{0.8\%}$ and $N_{c,max}$ is almost linear under these regimes. Such a linear relationship can be attributed to a narrow range of S_{eff} in each regime. Under the updraft-limited regime, for example, S_{eff} is ranged between 0.1 and 0.2, and thus $N_{c,max}$ should be proportional to N_{CCN} at the supersaturation between 0.1 and 0.2%. Because N_{CCN} in this range is almost linearly proportional to $N_{0.8\%}$, a near linear relationship was observed between $N_{0.8\%}$ and $N_{c,max}$. Similarly, under the aerosol-limited regime, S_{eff} ranged between 0.5 and 0.8, and an almost linear relationship was observed between $N_{0.8\%}$ and $N_{c,max}$ because N_{CCN} in the supersaturation range had a near linear relationship with $N_{0.8\%}$. As shown in Fig. 7, the $N_{0.8\%}$ - $N_{c,max}$ relationship for all cloud events is an aggregation of such near-linear relationships with various slopes, resulting in a relatively small ACI_N on the whole.

3.2. Favorable conditions for the aerosol-limited regime in Tokyo

Next, we examine the atmospheric conditions that favor the appearance of the aerosol-limited regime in Tokyo. Fig. 10 shows the mean values of the west to east (U_{975}) and the south to north (V_{975}) wind components at the 975-hPa level (corresponding to a height of approximately 300 m). The winds at this level are used, as this level is close in altitude to that of the observation site. The data are divided into four quadrants based on the wind direction (SW, SE, NE, NW). The occurrence of the aerosol-limited regime clearly depends on the wind direction (Fig. 10a). In the NW quadrant, 75.0% of the cases are classified as the aerosol-limited regime, while no aerosol-limited regime is observed in the SE quadrant. Such dependence on the wind direction is also observed in $N_{0.8\%}$ (Fig. 10b). In the NW and NE quadrants, for example, the mean values of $N_{0.8\%}$ are 451 cm^{-3} and 485 cm^{-3} , respectively, while in the SE and SW quadrants, they are 651 cm^{-3} and 833 cm^{-3} , respectively. These findings suggest that the aerosol-limited regime is more likely to occur when the number concentration of CCN is small.

This dependence of $N_{0.8\%}$ on wind direction is probably due to the presence of local pollution sources. As shown in Fig. 1, the area to the southwest of the observation site is a densely populated area, and there are pollution sources such as motor vehicles and factories. In addition, Tokyo Bay is located to the south of the observation site and aerosol particles may be supplied from the exhausts of ship engines. When the southerly wind component prevails, the air containing large amounts of aerosol is advected under the influence of such local pollution sources. On the other hand, the northern side of the observation site is less populated than the southern side. When the north wind component prevails, relatively clean air is transported to the observation site without being affected by the local pollution.

Fig. 11 shows the results of a backward trajectory analysis, which represents the trajectories of airmasses during 72 h prior to the onset of each cloud event. There is no significant difference among the three regimes; in all cases airmasses originated from the Pacific Ocean or mainland China, although the airmasses in the aerosol-limited regime tend to originate around Japan. This result suggests that long-range

transport of aerosols is not important for regime classification in ACI, but rather, that local wind direction is important.

Precipitation along the airmass trajectory can also affect the aerosol number concentration and hence the classification of ACI regimes through wet scavenging. In this study, 24-h and 72-h APT was examined, but only the results for the 24-h APT are shown (Fig. 12) because they showed stronger impacts. The mean value (10 mm) was used as a threshold, and the cloud events were divided into $APT \leq 10$ mm (22 cases) and $APT > 10$ mm (13 cases). The results show that the $APT \leq 10$ mm group has a larger mean $N_{0.8\%}$ and $N_{c,max}$ and a smaller S_{eff} than the $APT > 10$ mm group (Fig. 12). However, the results of t -tests showed that these differences were not statistically significant at the 95% confidence level. Therefore, it is suggested that APT does not have a significant effect on regime classification.

Next, the relationships among the regimes and temperature are examined. Fig. 13 shows the temperature at the 975-hPa level (T_{975} , units in $^{\circ}\text{C}$) on the horizontal axis and the potential temperature difference between the 1000-hPa and 950-hPa levels ($\Delta\theta_{950-1000}$) on the vertical axis. Here, $\Delta\theta_{950-1000}$ represents the atmospheric stability around the 975-hPa level, which is related to the updraft in clouds. The dashed lines indicate the mean values of T_{975} and $\Delta\theta_{950-1000}$ (18.8°C and 3.2 K , respectively), dividing the region into four quadrants (I–IV). The aerosol-limited regime occupies 70.0% of the quadrant with low temperature and low atmospheric stability (quadrant III). The mean S_{eff} in quadrant III is 0.51%, which is slightly larger than the threshold of the aerosol-limited regime (0.5%) and greater than the other quadrants (0.33%, 0.30% and 0.30% in quadrants I, II and IV, respectively). In this quadrant, the average value of $N_{0.8\%}$ is only 341 cm^{-3} (Fig. 13b). Because T_{975} was positively correlated with V_{975} (correlation coefficient 0.50, not shown), the small T_{975} reflects the prevalence of a northerly wind component. In addition, the lower atmospheric stability in quadrant III ($\Delta\theta_{950-1000} < 3.2 \text{ K}$) may reflect a stronger updraft and hence higher supersaturation. To summarize these results, the two independent parameters, V_{975} and $\Delta\theta_{975-1000}$, are combined to describe favorable conditions for the aerosol-limited regime using linear discriminant analysis (Fisher, 1936). We estimated the following inequality as:

$$V_{975} < 1.74 - 0.94\Delta\theta_{950-1000} \quad (10)$$

which indicates that the aerosol-limited regime in Tokyo is likely to appear when V_{975} and $\Delta\theta_{950-1000}$ are small (Fig. 14). The percentage of correct classification between the aerosol-limited regime and other regimes based on inequality (10) is 71.4%.

4. Summary and discussion

Regime classification of ACI was performed using the effective supersaturation for 35 cases of low-level clouds observed at the 458-m level of Tokyo Skytree. The results can be summarized as follows:

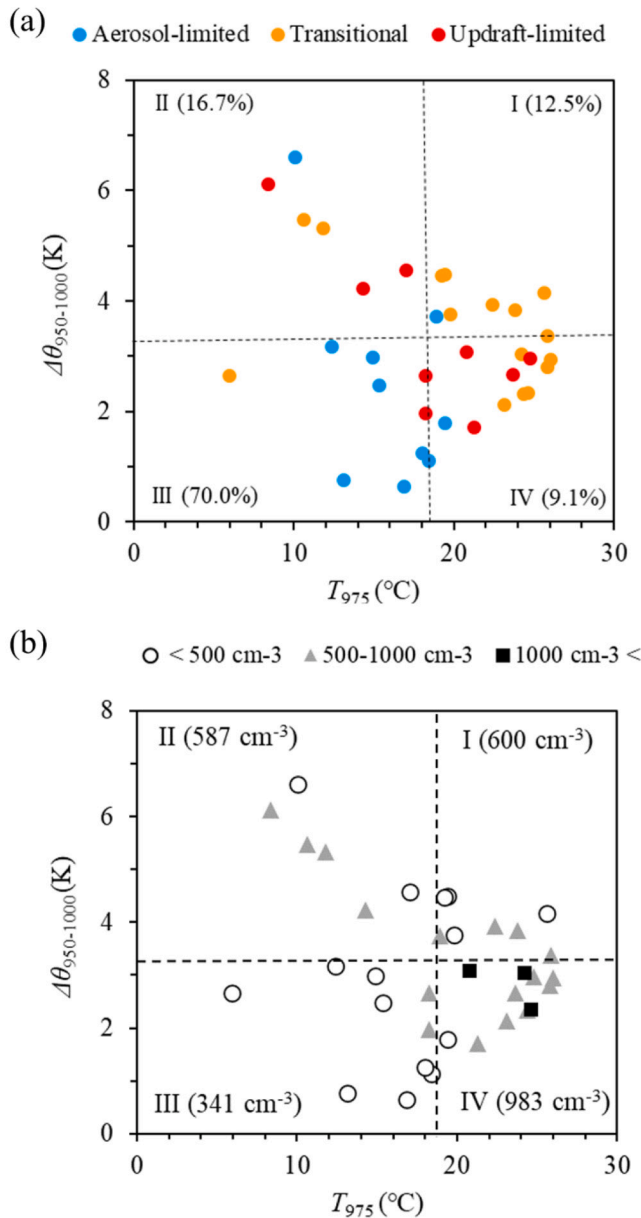


Fig. 13. Dependencies of (a) regime classification and (b) $N_{0.8\%}$ on the temperature at the 975-hPa level (T_{975}) and the atmospheric stability represented by the potential temperature difference between the 950 and the 1000-hPa levels ($\Delta\theta_{950-1000}$). The dashed lines indicate the mean values of T_{975} and $\Delta\theta_{950-1000}$. Numerals in parentheses are (a) percentage cases under the aerosol-limited regime and (b) mean values of $N_{0.8\%}$ in the quadrants bounded by the mean values.

- 1) Parcel model simulations showed that S_{eff} was well suited for use as a proxy indicator for S_{max} . One of the error sources of S_{eff} was variations in the CCN supersaturation spectrum due to airmass replacement.
- 2) Under the aerosol-limited regime, N_c increased and r_e decreased with increasing aerosols more rapidly than under the other two regimes, suggesting that the regime classification using S_{eff} was sufficiently robust.
- 3) The aerosol-limited regime in Tokyo tends to appear when the northerly wind component prevailed, and the atmospheric stability was low at the 975-hPa level. The dependence on the wind direction may have been due to the influence of local pollution around Tokyo to the south of the observation site, and the dependence on the

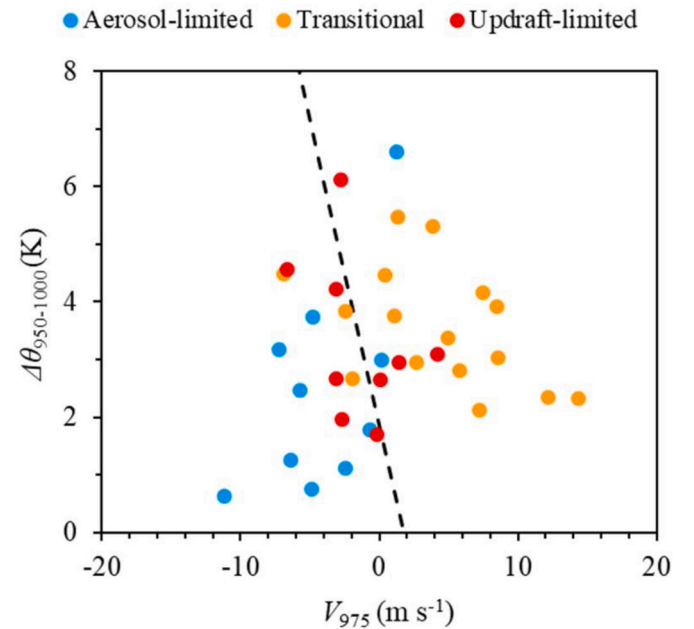


Fig. 14. Dependencies of regime classification on V_{975} and $\Delta\theta_{950-1000}$. The dashed lines indicate the discriminant lines between the aerosol-limited regime and the other regimes based on linear discriminant analysis.

atmospheric stability may have been related to the strength of updrafts in clouds.

The results obtained in this study showed that the aerosol indirect effect is quite active in Tokyo. According to satellite observations by Zhao et al. (2018a, 2018b), there is a region where AOT and r_e are strongly and negatively correlated in the North Pacific off the coast of the Japanese archipelago. Presumably, the air advected from this region is not polluted by industrial areas in Japan and contributes to the aerosol-limited regime in Tokyo. On the other hand, an aerosol-rich airmass has been reported over mainland China (e.g., Kim et al., 2007), but the aerosol particles originating from the continent did not have a marked influence on cloud properties in Tokyo, as the aerosol particles were more abundant when the southerly wind prevailed. However, the data used in this study were seasonally biased, and the effect of Asian dust events which occur frequently in spring was not examined.

The climate in Tokyo has changed significantly over the past century. The mean temperature has increased by 3 K (Matsumoto et al., 2017), afternoon precipitation has increased in summer (Fujibe et al., 2009), and the contribution of weak rainfall to total precipitation has decreased (Takahashi, 2003). While such long-term changes in precipitation are attributed mainly to the increase in sensible heat flux from the surface due to urbanization (Kusaka et al., 2014), the effect of cloud microphysics has not been studied extensively. In addition, a decrease in aerosol concentrations around Tokyo has been reported in recent years (Wakamatsu et al., 2013; Mori et al., 2020), and the aerosol-limited regime is expected to be more prevalent in the near future. This will likely influence the ACI over Tokyo and the climatological impact of these changes needs to be studied. Therefore, aerosol indirect effects on cloud properties in Tokyo, including precipitation and radiation, should be investigated in future.

Author statement

RM performed observations of cloud droplets, created the parcel model, wrote the paper, and prepared all figures; YU supported all observations and contributed to data curation; KM, TM, and YI performed

the CCN observations and data quality control; the particle transmission efficiency of the CCN observation system was calculated by TM; YT contributed to the observations and improved the paper with constructive comments. All authors have read and agreed to the published version of the manuscript.

Declaration of Competing Interest

The authors declare that they have no known competing financial interests or personal relationships that could have appeared to influence the work reported in this paper.

Acknowledgment

The authors sincerely thank Mr. Asato Maeda and Ms. Masami Yokoyama, former graduate students at the Tokyo University of Science, for their support with observations and analysis of CCN data. The XRAIN data used in this study were provided by the Ministry of Land, Infrastructure, Transport and Tourism through the Data Integration and Analysis System (DIAS). The authors gratefully acknowledge the NOAA Air Resources Laboratory (ARL) for the provision of the HYSPLIT transport and dispersion model and/or READY website (<https://www.ready.noaa.gov>) used in this study. This work was supported by JSPS KAKENHI (Grant Number JP21H01163).

Appendix A. Supplementary data

Supplementary data to this article can be found online at <https://doi.org/10.1016/j.atmosres.2022.106150>.

References

- Ahmad, I., Mielonen, T., Grosvenor, D.P., Portin, H.J., Arola, A., Mikkonen, S., Kühn, T., Leskinen, A., Joutsensaari, J., Komppula, M., 2013. Long-term measurements of cloud droplet concentrations and aerosol–cloud interactions in continental boundary layer clouds. *Tellus B* 65, 20138. <https://doi.org/10.3402/tellusb.v65i0.20138>.
- Albrecht, B.A., 1989. Aerosols, cloud microphysics, and fractional cloudiness. *Science* 245, 1227–1230. <https://doi.org/10.1126/science.245.4923.1227>.
- Ansari, K., Pandithurai, G., Kumar, V.A., 2020. Role of droplet size classes on the cloud droplet spectral dispersion as observed over the Western Ghats. *Atmos. Res.* 246, 105104 <https://doi.org/10.1016/j.atmosres.2020.105104>.
- Borys, R.D., Lowenthal, D.H., Cohn, S.A., Brown, W.O., 2003. Mountaintop and radar measurements of anthropogenic aerosol effects on snow growth and snowfall rate. *Geophys. Res. Lett.* 30 <https://doi.org/10.1029/2002GL016855>.
- Cai, Z., Li, Z., Li, P., Li, J., Sun, H., Gao, X., Peng, Y., Wang, Y., Zhang, D., Ren, G., 2022. Vertical distributions of aerosol and cloud microphysical properties and the aerosol impact on a continental cumulus cloud based on aircraft measurements from the Loess Plateau of China. *Frontiers in Environmental Science* 9. <https://doi.org/10.3389/fenvs.2021.808861>.
- Dadashazar, H., Alipanah, M., Hilario, M.R.A., Crosbie, E., Kirschler, S., Liu, H., Moore, R.H., Peters, A.J., Scarino, A.J., Shook, M., Thornhill, K.L., Voigt, C., Wang, H., Winstead, E., Zhang, B., Ziemba, L., Sorooshian, A., 2021. Aerosol responses to precipitation along north American air trajectories arriving at Bermuda. *Atmos. Chem. Phys.* 21, 16121–16141. <https://doi.org/10.5194/acp-21-16121-2021>.
- Feingold, G., Remer, L.A., Ramaprasad, J., Kaufman, Y.J., 2001. Analysis of smoke impact on clouds in Brazilian biomass burning regions: an extension of Twomey's approach. *J. Geophys. Res. Atmos.* 106, 22907–22922. <https://doi.org/10.1029/2001JD000732>.
- Fisher, R.A., 1936. The use of multiple measurements in taxonomic problems. *Ann. Eugenics* 7, 179–188. <https://doi.org/10.1111/j.1469-1809.1936.tb02137.x>.
- Fujibe, F., Togawa, H., Sakata, M., 2009. Long-term change and spatial anomaly of warm season afternoon precipitation in Tokyo. *SOLA* 5, 17–20. <https://doi.org/10.2151/sola.2009-005>.
- Godoy, H., Naito, M., Tsuchiya, S., 2014. Improvement of the observation accuracy of X-band dual polarimetric radar by expansion of the condition to use KDP-R relationship. *J. Jpn. Soc. Civ. Eng., Ser. B1 (Hydraul. Eng.)* 70. https://doi.org/10.2208/jscejhe.70.1_505 (1.505–1.510, in Japanese).
- Hammer, E., Bukowiecki, N., Gysel, M., Jurányi, Z., Hoyle, C.R., Vogt, R., Baltensperger, U., Weingartner, E., 2014. Investigation of the effective peak supersaturation for liquid-phase clouds at the high-alpine site Jungfraujoch, Switzerland (3580 m asl). *Atmos. Chem. Phys.* 14, 1123–1139. <https://doi.org/10.5194/acp-14-1123-2014>.
- Hudson, J.G., Noble, S., 2014. CCN and vertical velocity influences on droplet concentrations and supersaturations in clean and polluted stratus clouds. *J. Atmos. Sci.* 71, 312–331. <https://doi.org/10.1175/JAS-D-13-086.1>.
- Iwamoto, Y., Kinouchi, K., Watanabe, K., Yamazaki, N., Matsuki, A., 2016. Simultaneous measurement of CCN activity and chemical composition of fine-mode aerosols at Noto peninsula, Japan, in autumn 2012. *Aerosol Air Qual. Res.* 16, 2107–2118. <https://doi.org/10.4209/aaqr.2015.09.0545>.
- Iwamoto, Y., Watanabe, A., Kataoka, R., Uematsu, M., Miura, K., 2021. Aerosol–cloud interaction at the summit of Mt. Fuji, Japan: Factors influencing cloud droplet number concentrations. *Appl. Sci.* 11, 8439. <https://doi.org/10.3390/app1188439>.
- Jia, H., Ma, X., Yu, F., Liu, Y., Yin, Y., 2019. Distinct impacts of increased aerosols on cloud droplet number concentration of stratus/stratocumulus and cumulus. *Geophys. Res. Lett.* 46, 13517–13525. <https://doi.org/10.1029/2019GL085081>.
- Khvorostyanov, V.I., Curry, J.A., 2006. Aerosol size spectra and CCN activity spectra: Reconciling the lognormal, algebraic, and power laws. *J. Geophys. Res.* 111, D12202. <https://doi.org/10.1029/2005JD006532>.
- Kim, S.-W., Yoon, S.-C., Kim, J., Kim, S.-Y., 2007. Seasonal and monthly variations of columnar aerosol optical properties over East Asia determined from multi-year MODIS, LIDAR, and AERONET Sun/sky radiometer measurements. *Atmos. Environ.* 41, 1634–1651. <https://doi.org/10.1016/j.atmosenv.2006.10.044>.
- Kondo, Y., Takegawa, N., Matsui, H., Koike, M., Miyazaki, Y., Kanaya, Y., Mochida, M., Kuwata, M., Morino, Y., Shiraiwa, M., 2010. Formation and transport of aerosols in Tokyo in relation to their physical and chemical properties: a review. *J. Meteorol. Soc. Jpn.* 88, 597–624. <https://doi.org/10.2151/jmsj.2010-401>.
- Koren, I., Dagan, G., Altaratz, O., 2014. From aerosol-limited to invigoration of warm convective clouds. *Science* 344, 1143–1146. <https://doi.org/10.1126/science.1252595>.
- Kulkarni, P., Baron, P.A., Willeke, K., 2011. *Aerosol Measurement: Principles, Techniques, and Applications*. John Wiley & Sons, Inc.
- Kusaka, H., Nawata, K., Suzuki-Parker, A., Takane, Y., Furuhashi, N., 2014. Mechanism of precipitation increase with urbanization in Tokyo as revealed by ensemble climate simulations. *J. Appl. Meteorol. Climatol.* 53, 824–839. <https://doi.org/10.1175/JAMC-D-13-065.1>.
- Kuwata, M., Kondo, Y., 2008. Dependence of size-resolved CCN spectra on the mixing state of nonvolatile cores observed in Tokyo. *J. Geophys. Res. Atmos.* 113 <https://doi.org/10.1029/2007JD009761>.
- Li, J.R., Zhu, C., Chen, H., Zhao, D.F., Xue, L.K., Wang, X.F., Li, H.Y., Liu, P.F., Liu, J.F., Zhang, C.L., Mu, Y.J., Zhang, W.J., Zhang, L.M., Herrmann, H., Li, K., Liu, M., Chen, J.M., 2020. The evolution of cloud and aerosol microphysics at the summit of Mt. Tai, China. *Atmos. Chem. Phys.* 20, 13735–13751. <https://doi.org/10.5194/acp-20-13735-2020>.
- Matsumoto, J., Fujibe, F., Takahashi, H., 2017. Urban climate in the Tokyo metropolitan area in Japan. *J. Environ. Sci.* 59, 54–62. <https://doi.org/10.1016/j.jes.2017.04.012>.
- McComiskey, A., Feingold, G., 2012. The scale problem in quantifying aerosol indirect effects. *Atmos. Chem. Phys.* 12, 1031–1049. <https://doi.org/10.5194/acp-12-1031-2012>.
- Misumi, R., Uji, Y., Tobo, Y., Miura, K., Uetake, J., Iwamoto, Y., Maesaka, T., Iwanami, K., 2018. Characteristics of droplet size distributions in low-level stratiform clouds observed from Tokyo Skytree. *J. Meteorol. Soc. Jpn.* 96, 405–413. <https://doi.org/10.2151/jmsj.2018-040>.
- Miura, K., 2021. Variation of atmospheric aerosol particles over the Central Tokyo. *Archiv. Atmosph. Chem. Res.* 45, 045A03 (in Japanese). https://jpsac.org/wordpress/wp-content/uploads/2021/07/AACR_vol45.pdf.
- Miura, K., Sekikawa, T., 1990. Variation of concentration of ambient aerosols in Tokyo. *Atmos. Environ. Part A, General Topics* 24, 1401–1407. [https://doi.org/10.1016/0960-1686\(90\)90047-Q](https://doi.org/10.1016/0960-1686(90)90047-Q).
- Mochida, M., Kuwata, M., Miyakawa, T., Takegawa, N., Kawamura, K., 2006. Relationship between hygroscopicity and cloud condensation nuclei activity for urban aerosols in Tokyo. *J. Geophys. Res. Atmos.* 111, D23204. <https://doi.org/10.1029/2005JD006980>.
- Mori, T., Ohata, S., Morino, Y., Koike, M., Moteki, N., Kondo, Y., 2020. Changes in black carbon and PM_{2.5} in Tokyo in 2003–2017. *Proc. Jpn. Acad. Ser. B* 96, 122–129. <https://doi.org/10.2183/pjab.96.010>.
- Ohata, S., Schwarz, J.P., Moteki, N., Koike, M., Takami, A., Kondo, Y., 2016. Hygroscopicity of materials internally mixed with black carbon measured in Tokyo. *J. Geophys. Res. Atmos.* 121, 362–381. <https://doi.org/10.1002/2015JD024153>.
- Oliver, D.A., Lewellen, W.S., Williamson, G.G., 1978. The interaction between turbulent and radiative transport in the development of fog and low-level stratus. *J. Atmos. Sci.* 35, 301–316. [https://doi.org/10.1175/1520-0469\(1978\)035<0301:TIBTAR>2.0.CO;2](https://doi.org/10.1175/1520-0469(1978)035<0301:TIBTAR>2.0.CO;2).
- Orikasa, N., Saito, A., Yamashita, K., Tajiri, T., Zaizen, Y., Kuo, T.-H., Kuo, W.-C., Murakami, M., 2020. Seasonal variations of atmospheric aerosol particles focused on cloud condensation nuclei and ice nucleating particles from ground-based observations in Tsukuba, Japan. *SOLA*, vol. 16, pp. 212–219. <https://doi.org/10.2151/sola.2020-036>.
- Peters, M.D., Kreidenweis, S.M., 2007. A single parameter representation of hygroscopic growth and cloud condensation nucleus activity. *Atmos. Chem. Phys.* 7, 1961–1971. <https://doi.org/10.5194/acp-7-1961-2007>.
- Portin, H.J., Komppula, M., Leskinen, A.P., Romakkaniemi, S., Laaksonen, A., Lehtinen, K.E., 2009. Observations of aerosol–cloud interactions at the Puijo semi-urban measurement station. *Boreal Environ. Res.* 14, 641–653. <https://helda.helsinki.fi/bitstream/handle/10138/233541/ber14-4-641.pdf?sequence=1>.
- Reutter, P., Su, H., Trentmann, J., Simmel, M., Rose, D., Gunthe, S.S., Wernli, H., Andreae, M.O., Pöschl, U., 2009. Aerosol-and updraft-limited regimes of cloud droplet formation: influence of particle number, size and hygroscopicity on the activation of cloud condensation nuclei (CCN). *Atmos. Chem. Phys.* 9, 7067–7080. <https://doi.org/10.5194/acp-9-7067-2009>.

- Roberts, G.C., Nenes, A., 2005. A continuous-flow streamwise thermal-gradient CCN chamber for atmospheric measurements. *Aerosol Sci. Technol.* 39 (3), 206–221. <https://doi.org/10.1080/027868290913988>.
- Rolph, G., Stein, A., Stunder, B., 2017. Real-time environmental applications and display sYstem: READY. *Environ. Model Softw.* 95, 210–228. <https://doi.org/10.1016/j.envsoft.2017.06.025> this link opens in a new window.
- Rosenfeld, D., 2000. Suppression of rain and snow by urban and industrial air pollution. *Science* 287, 1793–1796. <https://doi.org/10.1126/science.287.5459.1793>.
- Rothenberg, D., Wang, C., 2016. Metamodeling of droplet activation for global climate models. *J. Atmos. Sci.* 73, 1255–1272. <https://doi.org/10.1175/JAS-D-15-0223.1>.
- Spiegel, J.K., Zieger, P., Bukowiecki, N., Hammer, E., Weingartner, E., Eugster, W., 2012. Evaluating the capabilities and uncertainties of droplet measurements for the fog droplet spectrometer (FM-100). *Atmos. Meas. Tech.* 5, 2237–2260. <https://doi.org/10.5194/amt-5-2237-2012>.
- Stein, A.F., Draxler, R.R., Rolph, G.D., Stunder, B.J.B., Cohen, M.D., Ngan, F., 2015. NOAA's HYSPLIT atmospheric transport and dispersion modeling system. *Bull. Amer. Meteor. Soc.* 96, 2059–2077. <https://doi.org/10.1175/BAMS-D-14-00110.1>.
- Stevens, B., Feingold, G., 2009. Untangling aerosol effects on clouds and precipitation in a buffered system. *Nature* 461, 607–613. <https://doi.org/10.1038/nature08281>.
- Takahashi, H., 2003. Seasonal variation in the occurrence property of summertime daily rainfall amount in and around the Tokyo Metropolitan area. *Tenki* 50, 31–41 (in Japanese). https://www.metsoc.jp/tenki/pdf/2003/2003_01_0031.pdf.
- Tobo, Y., Uetake, J., Matsui, H., Moteki, N., Uji, Y., Iwamoto, Y., Miura, K., Misumi, R., 2020. Seasonal trends of atmospheric ice nucleating particles over Tokyo. *J. Geophys. Res. Atmos.* 125 <https://doi.org/10.1029/2020JD033658> e2020JD033658.
- Twomey, S., 1974. Pollution and the planetary albedo. *Atmos. Environ.* 8, 1251–1256. [https://doi.org/10.1016/0004-6981\(74\)90004-3](https://doi.org/10.1016/0004-6981(74)90004-3).
- Uetake, J., Tobo, Y., Uji, Y., Hill, T.C., DeMott, P.J., Kreidenweis, S.M., Misumi, R., 2019. Seasonal changes of airborne bacterial communities over Tokyo and influence of local meteorology. *Front. Microbiol.* 10, 1572. <https://doi.org/10.3389/fmicb.2019.01572>.
- Wakamatsu, S., Morikawa, T., Ito, A., 2013. Air pollution trends in Japan between 1970 and 2012 and impact of urban air pollution countermeasures. *Asian. J. Atmos. Environ.* 7, 177–190. <https://doi.org/10.5572/ajae.2013.7.4.177>.
- Yang, F., McGraw, R., Luke, E.P., Zhang, D., Kollias, P., Vogelmann, A.M., 2019. A new approach to estimate supersaturation fluctuations in stratocumulus cloud using ground-based remote-sensing measurements. *Atmos. Meas. Tech.* 12, 5817–5828. <https://doi.org/10.5194/amt-12-5817-2019>.
- Zhao, X., Liu, Y., Yu, F., Heidinger, A.K., 2018a. Using long-term satellite observations to identify sensitive regimes and active regions of aerosol indirect effects for liquid clouds over global oceans. *J. Geophys. Res. Atmos.* 123, 457–472. <https://doi.org/10.1002/2017JD027187>.
- Zhao, C., Qiu, Y., Dong, X., Wang, Z., Peng, Y., Li, B., Wu, Z., Wang, Y., 2018b. Negative aerosol-cloud re relationship from aircraft observations over Hebei. China. *Earth and Space Science* 5, 19–29. <https://doi.org/10.1002/2017EA000346>.